CRYSTAL GROWTH & DESIGN

pubs.acs.org/crystal

Article

Salts of Tetraselenatetracene and Bis(ethylenedithio)tetrathiafulvalene with Metal Hexafluoroacetylacetonate Anions: $Mn^{II}(hfac)_3^-$, $Co^{II}(hfac)_2Cl^-$, and $Pr^{III}(hfac)_4^-$

Alexandra M. Flakina, Dmitry I. Nazarov, Maxim A. Faraonov, Aleksey V. Kuzmin, Eleonora I. Khasanova, Ilya A. Yakushev, Vladimir N. Zverev, Akihiro Otsuka, Hiroshi Kitagawa, and Dmitri V. Konarev*

Cite This: *Cryst. Growth Des.* 2025, 25, 6332−6344

Read Online

ACCESS | Metrics & More | Article Recommendations | Supporting Information

ABSTRACT: Oxidation of tetraselenatetracene (TSeT) and bis(ethylenedithio)-tetrathiafulvalene (BEDT-TTF) by *p*-chloranil in the presence of metal hexafluoroacetylacetonates: $Mn^{II}(hfac)_2$, $Co^{II}(hfac)_2$ and $Pr^{III}(hfac)_3$ followed by precipitation of crystals by *n*-hexane produces $(TSeT_{1.5})^+\{Mn^{II}(hfac)_3^-\}$ (**1**), $(TSeT_{1.5})^+\{Pr^{III}(hfac)_4^-\}$ (**3**), $(TSeT_2)^+\{Co^{II}(hfac)_2Cl^-\}$ (**4**), and $(ET_3)^+\{Mn^{II}(hfac)_3^-\}$ (**5**). Thioindigo dye is introduced into $(TSeT_{1.5})^+$ $(Thioindigo_{1.5})\{Mn^{II}(hfac)_3^-\}$ (**2**) due to the appearance of specific C═O···(Se−Se bond) interactions accompanied by the formation of short O···Se contacts of 2.85−3.04 Å length. Formal charges on TSeT are +0.666 and +0.5 in **1**-**3**, and **4**, respectively, and +0.333 on BEDT-TTF in **5**. Crystal structures and optical and magnetic properties were studied for **1**−**5**, and conductivity measurements and zone structure calculations were carried out for **3**. Salts **1**−**4** contain 1D stacks formed by TSeT, and salt **5** contains 2D layers formed by BEDT-TTF. Essential dimerization yields alternation of dimers and monomers within the stacks. Positive charges are localized on the dimers, which transfer to a diamagnetic singlet state in **1**, **2**, and **4**, preserving this state up to room temperature (RT). Only in **3** with weakly dimerized TSeT stacks positive charge is localized on both monomers and dimers, and the triplet state of the dimers is populated above 180 K (the singlet−triplet gap is 420 K). As a result, semiconducting behavior is observed for the oriented single crystal of **3** with the activation energy of 83 meV. According to the length of the central C═C bond in BEDT-TTF, charge separation is observed in the layers of **5**. As a result, neutral BEDT-TTF molecules surround $BEDT\text{-}TTF^{\bullet+}$. High-spin $Mn^{II}(hfac)_3^-$ anions (S = 5/2) in **1** and **2** have no exchange due to long distances between them and the absence of spins on the TSeT sublattice. The Co^{II} ions in $Co^{II}(hfac)_2Cl^-$ (**4**) have a square pyramid surrounding and show a rather high zero field splitting parameter D of 80 cm^{-1}. Despite that, slow magnetic relaxation is not observed in the 1−1500 Hz range. The $Pr^{III}(hfac)_4^-$ anions with the $^3H_4$ state for Pr^{III} in **3** show rather strong antiferromagnetic coupling of spins, and most probably $TSeT^{\bullet+}$ monomers are also involved in this coupling. The $Mn^{II}(hfac)_3^-$ anions are isolated in **5**, whereas weak antiferromagnetic coupling of spins is observed between $BEDT\text{-}TTF^{\bullet+}$ within the layers with an estimated exchange interaction characterized by J = −3.17 cm^{-1}.

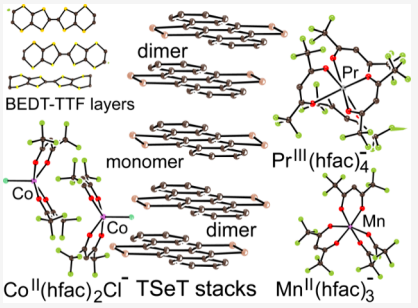

INTRODUCTION

An important task of modern science is the development of multifunctional materials.[1,2] Conducting materials can be prepared via the oxidation or reduction of organic or organometallic molecules. Conductivity can vary from semiconducting properties to metallic conductivity, and finally, superconductivity can also appear in some cases.[3−5] Molecular magnets and single-ion magnets (SIM) are prepared based on organic molecules and paramagnetic metals, and this field of research has successfully been developed.[6−9]

The combination of oxidized organic molecules with paramagnetic ions can provide the coexistence of conductivity with magnetic ordering of spins or SIM properties. Previously, giant magnetoresistance was observed in some molecular conductors that allowed the magnetic field to influence the conductivity.[10] Oxidized bis(ethylenedithio)tetrathiafulvalene (BEDT-TTF) or bis(ethylenedioxy)tetrathiafulvalene (BEDO-TTF) and $M(dmit)_2$, where dmit is 4,5-dimercapto-1,3-dithiole-2-dithione, were cocrystallized with anions and cations showing SIM properties and containing Re^{IV}, $Mn^{II/III}$, and

Received: May 22, 2025
Revised: July 10, 2025
Accepted: July 11, 2025
Published: July 23, 2025

Co^{II}.[11−15] In several examples, these compounds can show metallic-type conductivity and SIM properties at very low temperatures. Lanthanide-based SIMs are also promising for use in combination with oxidized or reduced organic molecules, which can manifest conductivity. Previously, we combined BEDT-TTF with Ho, Dy, and Tb chlorides, but no SIM properties were found.[16] Electrocrystallization was used to combine magnetic chains composed of Dy^{III} and BEDT-TTF layers to prepare SIMs with semiconducting properties.[17]

Metal hexafluoroacetylacetonates and anions based on them are also promising building blocks to prepare functional metal−organic compounds. It is known that metal(II) hexafluoroacetylacetonates can form complexes and coordination polymers even with weakly coordinating molecules such as oxygen-containing nitronyl-nitroxide radical ligands and some other ligands.[18−20] Manganese(II) and copper(II) hexafluoroacetylaacetonates form complexes with photochromic spiropyrans showing a transition to a high-spin state or field-induced SIM properties. Some of them are partially photoswitchable.[21,22] Some of the lanthanide metal hexafluoroacetylaceronates show SIM poperties[23,24] and can be promising magnetic building blocks when combined with photochromic cations[25] or conducting components. The latter possibility was realized in the recently obtained $\{TSeT_{1.5}\}^{\bullet+}[Dy^{III}(hfac)_4]^-$ salt (TSeT: tetraselenatetracene), which combines the 1D semiconducting TSeT stacks and field-induced SIM for the $[Dy^{III}(hfac)_4]^-$ anion with U_{eff} = 40.2 cm^{-1}.[26]

In this work, a synthetic strategy developed for the preparation of $\{TSeT_{1.5}\}^{\bullet+}[Dy^{III}(hfac)_4]^-$ was modified to prepare TSeT and bis(ethylenedithio)tetrathiafulvalene (BEDT-TTF) salts with other metal hexafluoroacetylacetonate anions. Molecules were oxidized in the presence of metal hexafluoroacetylacetonates of Mn^{II}, Co^{II}, and Pr^{III}. Five new salts: $(TSeT_{1.5})^+\{Mn^{II}(hfac)_3^-\}$ (**1**), $(TSeT_{1.5})^+(Thioindigo_{1.5})\{Mn^{II}(hfac)_3^-\}$ (**2**); $(TSeT_{1.5})^+\{Pr^{III}(hfac)_4^-\}$ (**3**); $(TSeT_2)^+\{Co^{II}(hfac)_2Cl^-\}$ (**4**) and $(ET_3)^+\{Mn^{II}(hfac)_3^-\}$ (**5**) were obtained as high-quality single crystals. We studied the crystal structures of these salts; their optical and magnetic properties. We also carried out conductivity measurements and DFT calculations for **3**. Partially oxidized TSeT and BEDT-TTF molecules form 1D stacks or 2D layers, respectively, and they coexist with bulky paramagnetic $Mn^{II}(hfac)_3^-$, $Co^{II}(hfac)_2Cl^-$, and $Pr^{III}(hfac)_4^-$ anions. This approach allows us to introduce paramagnetic anions into the salts containing potentially conducting stacks or layers of partially oxidized TSeT and BEDT-TTF. We also estimated the synthetic potential of the developed technique to generate radical cation salts with paramagnetic metal hexafluoroacetylacetonate anions, some of which can have SIM properties.

EXPERIMENTAL SECTION

Materials. Tetraselenatetracene (TSeT)[27] purified by sublimation, was used. BEDT-TTF was purchased from TCI. Starting anhydrous $Pr^{III}(hfac)_3$ was purchased from Strem. *p*-Chloranil (QCl_4), $Mn^{II}(hfac)_2{\cdot}xH_2O$ and $Co^{II}(hfac)_2{\cdot}xH_2O$ were purchased from TCI. Hexafluoroacetylacetonates were dried under vacuum and heated for four h at 80−95 °C. The obtained powders were stored in a glovebox. Thioindigo was purchased from TCI. *o*-Dichlorobenzene ($C_6H_4Cl_2$) was distilled over CaH_2 under reduced pressure, and *n*-hexane was distilled over Na/benzophenone. The solvents were degassed and stored in a glovebox. All manipulations for the synthesis of **1**−**5** were carried out in an MBraun 150B-G glovebox with a controlled atmosphere, and the content of H_2O and O_2 was less than 1 ppm. The crystals were stored in the glovebox and were sealed in 2 mm quartz tubes under ambient pressure of argon for EPR and SQUID measurements. KBr pellets for IR- and UV−visible-NIR measurements were prepared in the glovebox.

Methods. UV−visible-NIR spectra were measured in KBr pellets on a PerkinElmer Lambda 1050 spectrometer in the 250−2500 nm range. FT-IR spectra were obtained using KBr pellets with a PerkinElmer Spectrum 400 spectrometer (400−7800 cm^{-1}). A Quantum Design MPMS-XL SQUID magnetometer was used to measure static magnetic susceptibilities of **1**−**5** in a magnetic field of 1000 Oe under cooling and heating conditions in the 300−1.9 K range. The sample holder contribution and core-temperature-independent diamagnetic susceptibility (χ_d) were subtracted from the experimental values. The χ_d values were estimated from the extrapolation of the data in the high-temperature range and fitting the data with the following expression: $\chi_M = C/(T - \Theta) + \chi_d$, where *C* is the Curie constant and Θ is the Weiss temperature. The dynamic magnetic properties of **3** were studied at 3.0 Oe AC field at 1−1500 Hz frequencies by a Quantum Design MPMS-5S SQUID magnetometer.

Synthesis. We used a diffusion technique to synthesize crystals of **1**−**5**. All components were dissolved, the solution was cooled down to room temperature, and filtered into a glass tube of 46 mL volume, and *n*-hexane (26 mL) was layered over the obtained solution. A certain amount of white powder remained on the filter.

For preparation of $(TSeT_{1.5})^+\{Mn^{II}(hfac)_3^-\}$ (**1**) as crystals, TSeT (26 mg, 0.048 mmol), QCl_4 (10.5 mg, 0.043 mmol), and $Mn^{II}(hfac)_2$ (20.0 mg, 0.043 mmol) were dissolved in 18 mL of *o*-dichlorobenzene during 1 day at 40 °C. The solution turned dark green-blue after stirring for 1 day. Slow interdiffusion of *n*-hexane and *o*-dichlorobenzene for 1.5 months yielded good-quality black crystals. The solvent was decanted from the crystals, and they were washed with *n*-hexane to give black plates in 43% yield. Compositions of the crystals were determined by X-ray diffraction analysis. All of the crystals had the same shape and color. The same unit cell parameters for several crystals tested from the synthesis indicated that only one crystal phase was formed. Microprobe analysis showed a Mn: Se = 1.0:6.2 ratio that is close to the determined composition. Composition of **1**: Calcd for M_r = 1977.65 g·mol^{-1}: C 33.78, H 1.01; Found: C 33.22, H 0.93.

The crystals of $(TSeT_{1.5})^+$ $(Thioindigo_{1.5})\{Mn^{II}(hfac)_3^-\}$(**2**) were prepared by the following procedure: TSeT (26 mg, 0.048 mmol), QCl_4 (10.5 mg, 0.043 mmol), and $Mn^{II}(hfac)_2$ (20.0 mg, 0.043 mmol) were dissolved in 18 mL of *o*-dichlorobenzene during 1 day at 40 °C. The solution turned dark green-blue after stirring for 1 day. Thioindigo was added (12.4 mg, 0.042 mmol), and after that, the color of the solution changed to dark red-green. Slow interdiffusion of *n*-hexane and *o*-dichlorobenzene for 1.5 months yielded good-quality black crystals. The solvent was decanted from the crystals, and they were washed with *n*-hexane to give violet plates in 52% yield. Compositions of the crystals were determined from X-ray diffraction analysis. All the crystals had the same shape and color. The same unit cell parameters for several crystals tested from the synthesis indicated that only one crystal phase formed. Microprobe analysis showed a Mn:S:Se = 1.0:3.1:6.0 ratio that is close to the determined composition. Composition of **2**: Calcd for M_r = 1930.75 g·mol^{-1}: C 41.02, H 1.40; Found: C 40.74, H 1.16.

For preparation of $(TSeT_{1.5})^+\{Pr^{III}(hfac)_4^-\}$ (**3**), TSeT (26 mg, 0.048 mmol), QCl_4 (10.5 mg, 0.043 mmol), and $Pr^{III}(hfac)_3$ (32.0 mg, 0.043 mmol) were dissolved in 18 mL of *o*-dichlorobenzene during 1 day at 40 °C. The solution turned dark green-blue after stirring for 1 day. Slow interdiffusion of *n*-hexane and *o*-dichlorobenzene for 1.5 months yielded good-quality black crystals. The solvent was decanted from the crystals, and they were washed with *n*-hexane to give black rulers in 53% yield. The composition of the crystals determined from X-ray diffraction was $(TSeT_{1.5})^+\{Pr^{III}(hfac)_4^-\}$ (**3**). All crystals had the same shape and color. The same unit cell parameters for several crystals tested from the synthesis indicated that only one crystal phase formed. Microprobe analysis showed a Pr: Se = 1.0:6.1 ratio that is close to

https://doi.org/10.1021/acs.cgd.5c00737
Cryst. Growth Des. 2025, 25, 6332−6344

Table 1. X-ray Diffraction Data for 1−5

compound	1	2	3	4	5
emp. formula	$C_{55.67}H_{20}F_{24}$ $Mn_{1.33}O_8Se_8$	$C_{66}H_{27}F_{18}$ $MnO_9S_3Se_6$	$C_{47}H_{16}F_{24}O_8Pr$ Se_6	$C_{46}H_{18}ClCoF_{12}O_4Se_8$	$C_{90}H_{54}F_{36}Mn_2O_{12}S_{48}$
M_r (g·mol^{-1})	1977.65	1930.75	1779.27	1588.66	3660.09
color and shape	black plate	violet plate	black ruler	black ruler	brown plate
crystal system	triclinic	triclinic	monoclinic	triclinic	monoclinic
space group	$P\bar{1}$	$P\bar{1}$	$P2_1/c$	$P\bar{1}$	$C2/c$
a (Å)	10.1818(5)	10.6924(5)	10.5120(5)	12.1682(8)	24.9993(9)
b (Å)	17.5633(10)	16.4774(8)	14.8396(11)	13.4964(12)	22.7800(7)
c (Å)	27.7849(16)	19.0328(9)	35.668(3)	16.3242(14)	46.362(3)
α (°)	72.039(5)	84.5301(17)	90	98.899(7)	90
β (°)	80.501(4)	80.7163(18)	108.936(6)	106.800(7)	104.337(5)
γ (°)	80.670(4)	78.8708(18)	90	108.252(7)	90
V (Å^3)	4628.8(5)	3240.0(3)	5262.8(6)	2347.0(4)	25,580(2)
Z	3	2	4	4	8
ρ_{calc} [g/cm^3]	2.128	1.979	1.645	2.248	1.901
μ [mm^{-1}]	5.124	3.782	5.214	6.720	1.091
$F(000)$	2818	1868	3364	1500	14656
T (K)	110(2)	100(2)	140(2)	110(2)	100(2)
max. 2Θ (°)	56.540	51.294	54.284	54.204	50.484
reflns measured	49878	36113	13,053	20,366	62,228
unique reflns	20229	12190	13,053	10,136	29,639
parameters	1382	984	831	662	1751
restraints	1447	246	834	633	2189
reflns[$F_0 > 2(F_0)$]	9846	6635	7898	5533	15,523
R_1 [$F_0 > 2\sigma(F_0)$]	0.1250	0.0496	0.0578	0.0782	0.0701
WR_2 (all data)	0.2817	0.1205	0.1021	0.1593	0.1470
G.O.F	1.021	0.997	0.898	1.095	1.062
CCDC number	2433185	2422843	2433184	2433183	2433186

the determined composition. Composition of **3**: Calcd for M_r = 1779.27g·mol^{-1}: C 31.70, H 0.00; Found: C 31.29, H 0.80.

For preparation of $(TSeT_2)^+\{Co^{II}(hfac)_2Cl^-\}$ (**4**) crystals, TSeT (26 mg, 0.048 mmol), QCl_4 (10.5 mg, 0.042 mmol), and anhydrous $Co^{II}(hfac)_2$ (19.6 mg, 0.042 mmol) were dissolved in 18 mL of *o*-dichlorobenzene during 1 day at 40 °C. The solution turned dark green-blue after stirring for 1 day. Slow interdiffusion of *n*-hexane and *o*-dichlorobenzene for 1 month yielded good-quality black crystals. The solvent was decanted from the crystals, and they were washed with *n*-hexane to give black rulers in 62% yield. The composition of the crystals determined from X-ray diffraction was $(TSeT_2)$-$\{Co^{II}(hfac)_2Cl\}$. All the crystals had the same shape and color. The same unit cell parameters for several crystals tested from the synthesis indicated that only one crystal phase formed. Microprobe analysis showed a Co:Se = 1.0:8.2 ratio that is close to the determined composition. Composition of **4**: Calcd for M_r = 1588.66 g·mol^{-1}: C 34.78, H 1.13; Found: C 34.29, H 1.07. The synthesis was repeated several times at three different temperatures of the starting solution (40, 60, and 80°), but only the crystals of phase **4** were obtained in these syntheses according to the unit cell parameters.

Crystals of $(BEDT\text{-}TTF_3)^+\{Mn^{II}(hfac)_3^-\}$ (**5**) were prepared by the following procedure: BEDT-TTF (16 mg, 0.042 mmol), QCl_4 (10.5 mg, 0.043 mmol), and $Mn^{II}(hfac)_2$ (20.0 mg, 0.043 mmol) were dissolved in 18 mL of *o*-dichlorobenzene during 1 day at 60 °C. The solution turned dark brown. After 1 month, good-quality, very thin yellow-brown plates were obtained in a 51% yield. The composition of the crystals determined from X-ray diffraction was $\{(BEDT\text{-}TTF_3)\{Mn^{II}(hfac)_3\}$ (**1**). Microprobe analysis showed a Mn: S = 1.0:23.6 ratio that is close to the determined composition. Composition of **5**: Calcd for M_r = 3660.09 g·mol^{-1}: C 29.53, H 1.47; Found: C 29.23, H 1.39.

Crystal Structure Determination. X-ray diffraction data for **1**, **3**−**5** were collected on an Oxford diffraction "Gemini-R" CCD diffractometer with graphite-monochromated MoK_α radiation using an Oxford Instrument Cryojet system, and for **2** on a D8 Venture diffractometer (Bruker, Germany) in the ϕ- and ω-scanning modes at the Center for Collective Use of the Kurnakov Institute of General and Inorganic Chemistry, the Russian Academy of Sciences (λ = 0.71073 Å, Incoatec IμS 3.0 microfocus X-ray source) (Table 1). Primary indexing, the refinement of unit cell parameters, and the integration of reflections were performed using the Bruker APEX3 software package.[28] Reflection intensity was corrected for absorption by using the SADABS software. The raw data were reduced to F^2 using CrysAlisPro (Oxford Diffraction Ltd.). The structures were solved via a direct method and refined through the full-matrix least-squares method against F^2 using SHELX-2018/3 and Olex2.[29,30] Non-hydrogen atoms were refined in the anisotropic approximation. Positions of the hydrogen atoms were calculated geometrically. One independent TSeT in **1** with half occupancy is statistically disordered between two orientations. Two CF_3 groups of $Mn^{II}(hfac)_3^-$ are disordered between two orientations in **2** with 0.75(3)/0.25(3) and 0.507(11)/0.493(11) occupancies. Two CF_3 groups of $Pr^{III}(hfac)_4^-$ are disordered between two orientations in **3** with 0.542(11)/0.458(11) and 0.506(9)/0.494(9) occupancies. One CF_3 group of $Co^{II}(hfac)_2Cl^-$ is disordered between two orientations in **4** with 0.68(2)/0.32(2) occupancies. One CF_3 group of $Mn^{II}(hfac)_3^-$ is disordered between two orientations in **5** with 0.646(6)/0.54(6) occupancies. Additionally, the $-CH_2-CH_2-$ group of BEDT-TTF is disordered between two positions with 0.754(13)/0.246(13) occupancies. To keep the anisotropic thermal parameters of the disordered atoms within reasonable limits, the displacement components were restrained using SHELXL instructions of ISOR, SIMU, and DELU. That resulted in 1447, 246, 834, 633, and 2189 restraints for the refinement of crystal structures of **1**−**5**, respectively (Table 1).

RESULTS AND DISCUSSION

Synthesis. A new approach was developed to obtain previously characterized $\{TSeT_{1.5}\}^{\bullet+}[Dy^{III}(hfac)_4]^-$.[26] In this work, we carried out the reaction of TSeT with $Pr^{III}(hfac)_3$ by using another oxidizer. One equivalent amount of *p*-chloranil

https://doi.org/10.1021/acs.cgd.5c00737
Cryst. Growth Des. 2025, 25, 6332−6344

(QCl_4), anhydrous $Pr^{III}(hfac)_3$, and a slight excess of TSeT were mixed in dry *o*-dichlorobenzene in anaerobic conditions for 24 h at 40 °C until complete dissolution of TSeT and the formation of a deep green-blue solution. Oxidation of TSeT by QCl_4 provides the formation of $TSeT^{\bullet+}$ radical cations and $QCl_4^{\bullet-}$ radical anions. We can suppose that, as in the previous case,[26] Pr^{III} can form a polymer with $QCl_4^{\bullet-}$ precipitating from the solution. Similar $La^{III}(TCNE)_3$ polymers are known with tetracyanoethylene.[31] The formation of polymer generates free $hfac^-$ ligands, which coordinate to $Pr^{III}(hfac)_3$, forming the $[Pr^{III}(hfac)_4]^-$ counteranions. Large size of $[Pr^{III}(hfac)_4]^-$ provides high enough solubility of this salt despite the poor solubility of $TSeT^{\bullet+}$ in organic solvents. The resulting reaction solution contains only $TSeT^{\bullet+}$ and $[Pr^{III}(hfac)_4]^-$ since only these species were found in the reaction products.

The preliminary reaction scheme is given below:

$$\begin{aligned} &3TSeT + 3QCl_4 + 3Pr^{III}(hfac)_3 \\ &\rightarrow 3TSeT^{\bullet+} + 3QCl_4^{\bullet-} + 3Pr^{III}(hfac)_3 \\ &\rightarrow Pr^{III}(QCl_4^{\bullet-})_3 \downarrow + 3TSeT^{\bullet+} + 2[Pr^{III}(hfac)_4]^- \\ &\quad + hfac^- \\ &\rightarrow \{TSeT_{1.5}\}^{\bullet+}[Pr^{III}(hfac)_4]^- \end{aligned} \quad (1)$$

As a result, $\{TSeT_{1.5}\}^{\bullet+}[Pr^{III}(hfac)_4]^-$ (**3**) was obtained as a good-quality single crystals. It is interesting that a similar synthesis with $Er^{III}(hfac)_3$ and TSeT does not produce any crystals.

We used hexafluoroacetylacetonates of two-valent metals such as Mn^{II}, Co^{II}, Ni^{II}, and Cu^{II} for further studies. Black single crystals were obtained only in the first two cases. The crystals have the following compositions: $(TSeT_{1.5})^+\{Mn^{II}(hfac)_3^-\}$ (**1**) and $(TSeT_2)^+\{Co^{II}(hfac)_2Cl^-\}$ (**4**). It is seen that the above-mentioned mechanism can be applied only for the synthesis with $Mn^{II}(hfac)_2$, whereas the $Co^{II}(hfac)_2Cl^-$ anion is most probably formed by the abstraction of the Cl^- anion by $Co^{II}(hfac)_2$ from solvent $C_6H_4Cl_2$ molecules. Previously, such abstraction was observed when metal-containing species were generated in *o*-$C_6H_4Cl_2$.[32] Syntheses with $Co^{II}(hfac)_2$ were repeated several times at different temperatures, but according to the unit cell parameters of the obtained single crystals, only the crystals of phase **4** were obtained in all cases. The replacement of the solvent by a nonchlorinated one, like toluene, is not possible due to the complete insolubility of this salt in this solvent. The use of $Ni^{II}(hfac)_2$ and $Cu^{II}(hfac)_2$ does not allow for the preparation of any crystals. To introduce the dye component into the salt, we added thioindigo to the synthesis with TSeT and $Mn^{II}(hfac)_2$. Indeed, this component was inserted into the salt due to the appearance of specific C═O···(Se−Se bond) interactions. Therefore, some dyes and other functional components can be introduced into the salts with selenium-containing donors. However, the presence of a Se−Se bond is needed in the donors for this reaction.

We also studied the oxidation of BEDT-TTF under similar conditions. Lanthanide-containing hexafluoroacetylacetonates cannot be used because BEDT-TTF is not oxidized under these conditions. The brown color of oxidized BEDT-TTF appears only when $Mn^{II}(hfac)_2$ is used, and yellow-brown crystals of $(BEDT\text{-}TTF_3)^+\{Mn^{II}(hfac)_3^-\}$ (**5**) are finally obtained after slow mixing with *n*-hexane. Interestingly, other cyano-containing acceptors such as dichlorodicyanobenzoquinone (DDQ) or tetracyanoethylene (TCNE) do not produce any crystalline products. Moreover, the use of other metal-containing acetylacetonates yields no crystals (like acetylacetonate or 2,2,6,6-tetramethyl-3,5-heptanedionate (TMHD).

The compositions of the obtained salts are shown in Table 2. It was confirmed by the EDX method on single crystals, which allows M : S, M : Se, or M : Se : S ratios to be determined for these salts (see experimental section).

Table 2. Composition of the Salts Obtained from the X-ray Diffraction Data

compound	composition	average charge on TSeT (BEDT-TTF)
1	$(TSeT_{1.5})^+\{Mn^{II}(hfac)_3^-\}$	+0.666
2	$(TSeT_{1.5})^+$ $(Thioindigo_{1.5})\{Mn^{II}(hfac)_3^-\}$	+0.666
3	$(TSeT_{1.5})^+\{Pr^{III}(hfac)_4^-\}$	+0.666
4	$(TSeT_2)^+\{Co^{II}(hfac)_2Cl^-\}$	+0.50
5	$(BEDT\text{-}TTF_3)^+\{Mn^{II}(hfac)_3^-\}$	+0.333

Optical Spectra. Optical spectra of **1**-**5** were studied in KBr pellets prepared under anaerobic conditions. The spectra in the 250−2000(2500) nm range for salts **1**, **4** and **5** are shown in Figure 1, whereas the spectra of **2**, **3** and $(TSeT_{1.5})^+\{Dy^{III}(hfac)_4^-\}$[26] are given for comparison in Supporting Information (SI) (Figures S6 and S7).

Spectra of salts **1**−**4** contain the same set of bands at 305−312, 426−457, 626−648, and 1230−1290 nm (Table 3, Figure 1a, b) ascribed to TSeT. The lowest energy band at 1230−1290 nm originates from $TSeT^{\bullet+}$. The bands at 307 and 598 nm are attributed to BEDT-TTF in the spectrum of **5**, with the lowest energy band of $BEDT\text{-}TTF^{\bullet+}$ at 920 nm (Figure 1c). Similar bands were previously observed in the salts containing $TSeT^{\bullet+}$ and $BEDT\text{-}TTF^{\bullet+}$ radical cations.[33−35] The spectrum of salt containing thioindigo dye shows an additional band at 548 nm, which is attributed to a neutral dye since this band is not shifted relative to that in the spectrum of starting thioindigo (547 nm).

In addition to the bands of the radical cations, we observed broad bands, which can be attributed to the charge transfer (CT) bands. CT is possible between TSeT and BEDT-TTF in the 1D stacks or 2D layers, respectively. Maxima of these bands are positioned in the 2320−3700 cm^{-1} range (2700−43100 nm) for TSeT salts, and therefore, they are not observed in the NIR spectra, which were measured up to 2500 nm. Nevertheless, these bands are observed at 2000−4000 cm^{-1} in the IR spectra (Figures S8−S12). The lowest energy band is observed at 2320 cm^{-1} for **3**, and a similar, even lower energy band was previously observed in $(TSeT_{1.5})^+\{Dy^{III}(hfac)_4^-\}$ at 1950 nm.[26] Correspondingly, CT bands appear at higher energies in other salts with a higher degree of dimerization.

The CT band is manifested at the highest energy (4700 cm^{-1}) for salt **5**, and it is well pronounced in the NIR spectrum at about 1900 nm (Figure 1c). Therefore, the CT excitations have the highest energy in **5**.

Crystal Structures. Crystal structures of **1**−**5** were solved at low temperatures and with slow cooling of the crystals. The discussed bond lengths for crystallographically independent TSeT and BEDT-TTF units are listed in Table 4.

$(TSeT_{1.5})^+\{Mn^{II}(hfac)_3^-\}$ (**1**) contains two crystallographically independent $\{Mn^{II}(hfac)_3^-\}$ anions, two whole and two halves of the TSeT molecules. 1.5TSeT per anion indicates a

https://doi.org/10.1021/acs.cgd.5c00737
Cryst. Growth Des. 2025, 25, 6332−6344

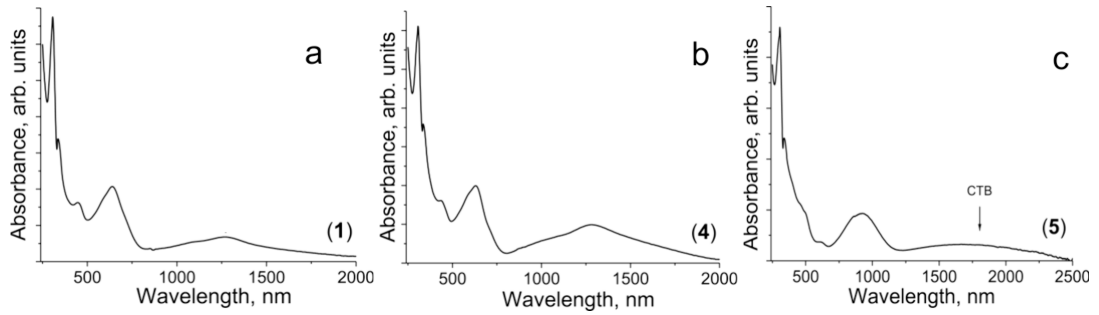

Figure 1. Spectra of: (a) $(TSeT_{1.5})^{+}\{Mn^{II}(hfac)_3^{-}\}$ (**1**); (b) $(TSeT_2)^{+}\{Co^{II}(hfac)_2Cl^{-}\}$ (**4**); and (c) $(BEDT\text{-}TTF_3)^{+}\{Mn^{II}(hfac)_3^{-}\}$ (**5**) in the UV−visible-NIR range in KBr pellets prepared in anaerobic conditions.

Table 3. Spectra of the Salts in the UV-Visible and Near-IR Ranges

compound	composition	UV−visible nm	CT bands near-IR, cm^{-1} (nm)
1	$(TSeT_{1.5})^{+}\{Mn^{II}(hfac)_3^{-}\}$	307, 450, 632, 1260	2620 cm^{-1} (3800 nm)
2	$(TSeT_{1.5})^{+}$ $(Thioindigo_{1.5})\{Mn^{II}(hfac)_3^{-}\}$	312, 448, 648, 1230, 548 (thioindigo)	3420 cm^{-1} (3000 nm)
3	$(TSeT_{1.5})^{+}\{Pr^{III}(hfac)_4^{-}\}$	305, 457, 647, 1265	2320 cm^{-1} (4310 nm)
	$(TSeT_{1.5})^{+}\{Dy^{III}(hfac)_4^{-}\}$ [24]	305, 457, 646, 1250	1950 cm^{-1} (5130 nm)
4	$(TSeT_2)^{+}\{Co^{II}(hfac)_2Cl^{-}\}$	309, 426, 626, 1290	3700 cm^{-1} (2700 nm)
5	$(BEDT\text{-}TTF_3)^{+}\{Mn^{II}(hfac)_3^{-}\}$	307, 598, 920	4700 cm^{-1} (~1900 nm, observed)

Table 4. Selected Bond Length for Crystallographically Independent TSeT and BEDT-TTF Molecules in 1−5

compound		Se−Se and central C=C bond length in TSeT, ET		
$TSeT^{0}$	[33]	2.339		
$TSeT^{\bullet+}$	[33,34]	2.322(3)		
1	1 ind.	2.323(2), 2.324(2)	2.315(3), 2.328(2)	dimers
	0.5 ind.	2.403(2)	disorder	monomers
2	1 ind.	2.320(1), 2.321(1)		dimer
	0.5 ind.	2.332(1)		monomer
3	1 ind.	2.3332(16), 2.3221(17)		dimer
	0.5 ind.	2.3289(15)		monomer
4	1 ind.	2.320(1), 2.325(1)		dimer
	0.5 ind.	2.335(1)		neutral monomer
	0.5 ind.	2.348(2)		neutral monomer
ET^{0}	[36]	1.352(1) for central C=C bond		
$ET^{\bullet+}$	[37]	1.397(3) for central C=C bond		
5 (ET)	0.5 ind.	1.388(6)	1.387(6)	$monomer^{\bullet+}$
	1 ind.	1.354(6)	1.346(6)	neutral molecule
	1 ind.	1.348(6)	1.345(6)	neutral molecule
	0.5 ind.	1.392(6)	1.392(6)	$monomer^{\bullet+}$

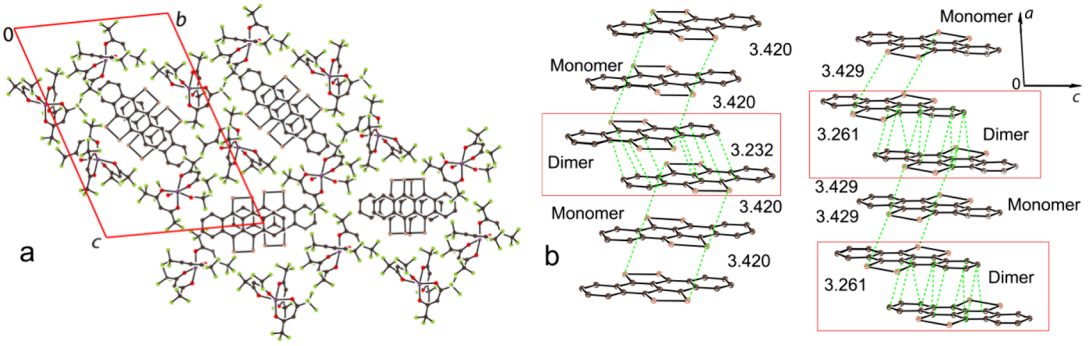

Figure 2. View on the crystal structure of $(TSeT_{1.5})^{+}\{Mn^{II}(hfac)_3^{-}\}$ (**1**) along the TSeT stacks (a) and on two different TSeT stacks arranged along the *a* axis (b). Dimers are shown by red rectangles.

formal +0.666 charge per TSeT. The TSeT molecules form stacks with π-stacking due to their parallel arrangement and short interplanar distances. Two types of stacks were found in **1**, which are completely isolated by bulky $\{Mn^{II}(hfac)_3^{-}\}$ anions (Figure 2a). Both types of stacks show essential dimerization since molecules with full occupancy form short

https://doi.org/10.1021/acs.cgd.5c00737
Cryst. Growth Des. 2025, 25, 6332−6344

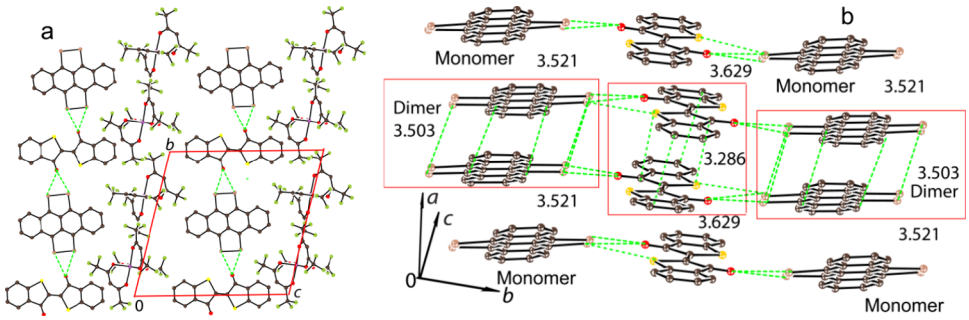

Figure 3. View on the crystal structure of $(TSeT_{1.5})^+$ $(Thioindigo_{1.5})\{Mn^{II}(hfac)_3^-\}$ (**2**) along the TSeT stacks (a) and on two different TSeT stacks arranged along the *a* axis (b). Dimers are shown by red rectangles.

interplanar distances of 3.232 and 3.261 Å, indicating the formation of dimers, whereas monomeric units formed by molecules with half occupancy are separated from the dimers by 3.420 and 3.429 Å interplanar distances. Many short van der Waals (vdW) contacts are formed in the dimers, and only two rather long contacts are formed between dimers and monomers (these contacts are shown by green dashed lines in Figure 2b). These results show an essential degree of dimerization of TSeT.

Positive charge on TSeT affects the Se−Se bond length since this bond is shortened nearly by 0.02 Å when one positive charge appears on TSeT (Table 4). The length of the Se−Se bonds in the monomers of **1** indicates the formation of neutral species, whereas the length of these bonds in the dimers indicates the positive charge of TSeT (Table 4). Therefore, besides dimerization, localization of positive charges on the dimers is observed. Six oxygen atoms coordinate to Mn^{II} in the $\{Mn^{II}(hfac)_3^-\}$ anions (Figure S13a). The length of Mn−O bonds is 2.12−2.17 Å. Analysis of the Mn^{II} surrounding in **1** by the Shape program[38,39] indicates that its geometry is closer to the octahedron with the O_h symmetry (Figure S13a). It is known that the H···F hydrogen bonds and the F···F contacts are important to stabilize crystal structures.[40,41] Indeed, many F···F contacts (2.92−2.79 Å) shorter than the sum of van der Waals radii of two fluorine atoms (2.94 Å) and short H···F hydrogen bonds (2.51−2.79 Å) are observed in the structure of **1.**

The addition of thioindigo during the synthesis allows the insertion of dye into the salt. There is one independent $Mn^{II}(hfac)_3^-$ anion, one and a half independent TSeT, and thioindigo molecules in **2**. Since thioindigo cannot be oxidized in contrast to TSeT, the positive charge is localized mainly on TSeT, and the formal charge on TSeT is +0.666. Specific interaction between TSeT and thioindigo involves the highly polarized donor Se−Se bond and acceptor C═O groups of thioindigo. This carbonyl oxygen atom approaches very close to the center of the Se−Se bond, forming very short O···Se contacts of 2.85−3.04 Å for both Se atoms involved in this bond. Potentially, such interactions allow the insertion of different dye molecules with carbonyl groups into the salts with donors containing electron-rich Se−Se bonds. Such a bonding is considered as a "chalcogen bonding".[42,43]

A layered structure is formed in **2** in which layers composed of $Mn^{II}(hfac)_3^-$ alternate with the those composed of TSeT and thioindigo stacks. Interplanar TSeT distances become closer to each other in the dimers, and between the dimers and monomers of 3.503 and 3.521 Å but the shortest distance in the dimers increases in comparison with that in **1** decreasing the number vdW contacts to four (Figure 3). At the same time due to longer interplanar distances and shift of TSeT molecules in the monomers and dimers no vdW contacts are formed between them. Charge on TSeT in the monomers is closer to the neutral state (2.332(1) Å), whereas TSeT molecules in the dimers are positively charged with the length of the Se−Se bonds of 2.320(1) Å. Therefore, dimerization and charge localization are seen in the TSeT stacks. It is interesting that stacks formed by thioindigo molecules are even stronger dimerized since the interplanar distance between thioindigo molecules in the dimers is 3.286 Å, whereas that between the dimers and monomers is 3.629 Å. As a result, short vdW contacts are formed only in the dimers. Geometry of $Mn^{II}(hfac)_3^-$ in **2** is close to that in **1**. There is only one F··· F contact of 2.84 Å length between the $Mn^{II}(hfac)_3^-$ anions, whereas many short H···F hydrogen bonds of 2.46−2.56 Å are observed in **2.**

Chlorine anions coordinate to $Co^{II}(hfac)_2$ forming $Co^{II}(hfac)_2Cl^-$ in **4** (Figure 4a). There are one independent

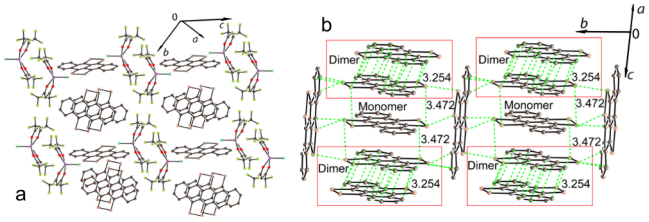

Figure 4. View on the crystal structure of $(TSeT_2)^+\{Co^{II}(hfac)_2Cl^-\}$ (**4**) along the TSeT layers (a) and on the TSeT layer (b). Dimers are shown by red rectangles.

$Co^{II}(hfac)_2Cl^-$ anion, one whole and two halves of independent TSeT molecules. There are two TSeT molecules per anion, and their formal charge of +0.50 is lower than those in **1**-**3**. The TSeT molecules form stacks which are separated by TSeT molecules positioned perpendicular to these stacks (Figure 4b). They form multiple contacts with the Se atoms of TSeT (Figure 4b). As a result, the layers containing TSeT alternate with those composed of the $\{Co^{II}(hfac)_2Cl^-\}_2$ dimers (Figure 4a). No vdW contacts are formed between $Co^{II}(hfac)_2Cl^-$ in the dimers since the interplanar distance between the hfac planes (4.17 Å) is long and they are shifted relative to each other. Strong dimerization is observed in the TSeT stacks since the interplanar distance in the dimers is 3.254 Å, whereas it is 3.472 Å between the dimers and monomers. As a result, 16 short vdW contacts are formed in the dimers and only two such contacts are formed between the dimers and monomers (green dashed lines in Figure 4b). It is

https://doi.org/10.1021/acs.cgd.5c00737
Cryst. Growth Des. 2025, 25, 6332−6344

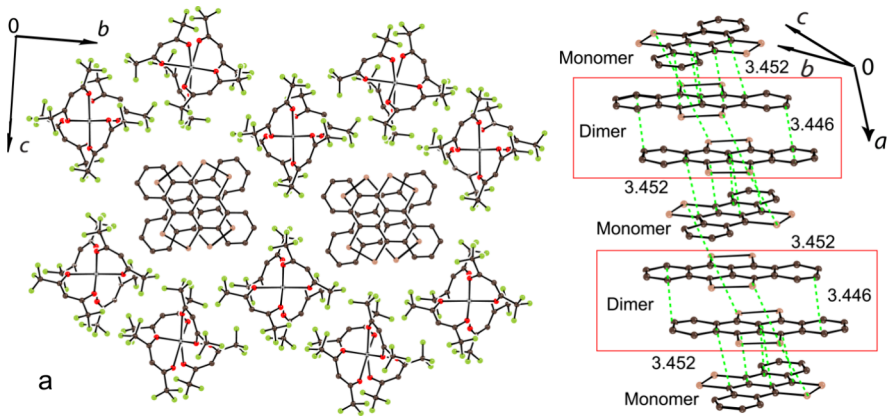

Figure 5. View on the crystal structure of $(TSeT_{1.5})^{+}\{Pr^{III}(hfac)_4^{-}\}$ (**3**) along the TSeT stacks (a) and on one TSeT stack arranged along the *a* axis (b). Dimers are colored red rectangles.

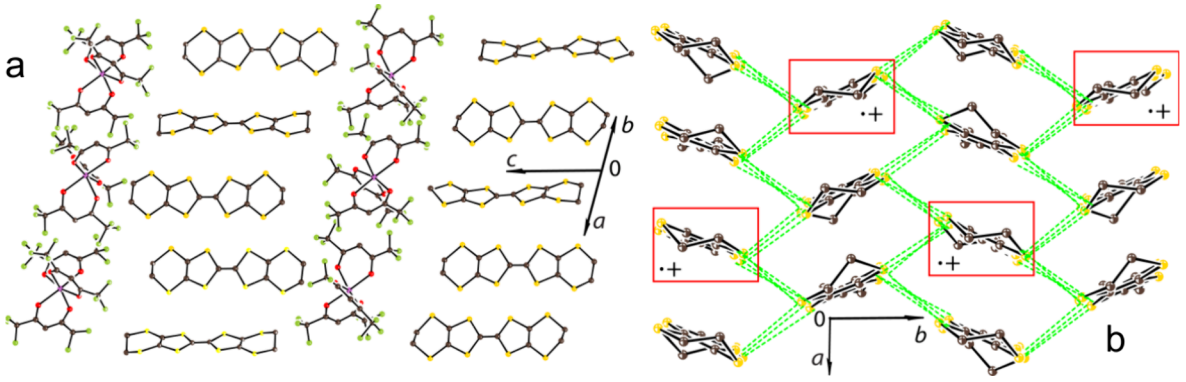

Figure 6. View on the crystal structure of $(BEDT\text{-}TTF_3)^{+}\{Mn^{II}(hfac)_3^{-}\}$ (**5**) along the BEDT-TTF layers (a) and on the BEDT-TTF layer approximately along the BEDT-TTF molecules (b). The $BEDT\text{-}TTF^{\bullet+}$ radical cations with elongated C═C bonds are shown by a red box.

seen from the length of the Se−Se bonds that TSeT molecules positioned in the perpendicular position to the stacks (3.320(1) Å) and in the TSeT monomers within the stacks (2.325(1) Å) are neutral, whereas TSeT molecules in the dimers have charge close to +1 (Table 4). Thus, dimerization and localization of positive charges on the dimers are observed in **4**. Co^{II} ions have spherical square pyramid geometry with the C_{4v} symmetry according to the Shape program[38,39] (Table S8), the length of O−Co bonds is 2.13−2.17 Å, and the Cl−Co bond is 2.356(4) Å (Figure S13b). Due to the presence of the $\{Co^{II}(hfac)_2Cl^{-}\}_2$ dimers, the F···F contacts shorter than 2.94 Å are absent in **4**, whereas there are many H···F hydrogen bonds of 2.41−2.72 Å length are formed.

There is one independent $Pr^{III}(hfac)_4^{-}$ anion and one and a half independent TSeT in **3**. That corresponds to +0.666 charge per TSeT molecule. Salt **3** is isostructural to previously described $(TSeT_{1.5})^{+}\{Dy^{III}(hfac)_4^{-}\}$[26] but has some peculiarities. TSeT molecules form weakly dimerized stacks surrounded by $Pr^{III}(hfac)_4^{-}$ (Figure 5a). They contain dimers and monomers with rather close interplanar distances of 3.446 and 3.452 Å (Figure 5b). As a result, the number of vdW contacts is 4−5 in the dimers and between the dimers and monomers (Figure 5b). The Se−Se bond length for TSeT in the dimers and monomers is close for the monomers and dimers (2.328(2) Å in average) and (2.329(2) Å), respectively (Table 4), indicating that the positive charge is delocalized between them in contrast to other studied complexes. Molecular structure of the $Pr^{III}(hfac)_4^{-}$ anions is shown in Figure S14. The Pr^{III} anions are surrounded by eight oxygen atoms with the length of the Pr−O bonds of 2.42−2.45 Å. Interestingly, the Dy−O bonds in $Dy^{III}(hfac)_4^{-}$ are noticeably shorter, being 2.32−2.36 Å.[26] According to the Shape program,[38,39] the Pr^{III} ions (Table S7) have a triangular dodecahedron surrounding them with the D_{2d} symmetry. Both H···F hydrogen bonds of 2.51−2.64 Å length and short F···F contacts of 2.74−2.91 Å length are observed in **3**.

To obtain salt **5**, oxidized BEDT-TTF molecules were cocrystallized with $Mn^{II}(hfac)_3^{-}$. There are one whole and two halves of independent $Mn^{II}(hfac)_3^{-}$ anions per four whole and four halves of BEDT-TTF molecules, indicating a formal +0.3333 charge on them. BEDT-TTF molecules form layers arranged in the *ab* plane and alternating with the anionic layers (Figure 6a). The BEDT-TTF layers can be attributed to the *θ*-type. View of the layers along the BEDT-TTF molecules is shown in Figure 5b. The length of the central C═C bond in BEDT-TTF is sensitive to its charge state, increasing from 1.352(1) Å for a neutral molecule to 1.397(3) Å for the radical cation.[36,37] Interplanar distances between BEDT-TTF are uniform. Nevertheless, considering the length of the central C═C bond in BEDT-TTF, it is seen that molecules with full occupancy are neutral (1.348(6) Å), whereas molecules with half occupancy have a positive charge (1.391(6) Å) (Table 4). As a result, charge localization is observed in the BEDT-TTF layers of **5**. Radical cations are positioned in such a way that they are surrounded in the layers mainly by neutral BEDT-TTF ($BEDT\text{-}TTF^{\bullet+}$ in the layers is shown by the red box in Figure 6b). Therefore, high conductivity is not expected in **5** despite the layered structure and partial formal charge on

https://doi.org/10.1021/acs.cgd.5c00737
Cryst. Growth Des. 2025, 25, 6332−6344

BEDT-TTF. Geometry of $Mn^{II}(hfac)_3^-$ in **5** is close to that in **1**. Both H···F hydrogen bonds of 2.45−2.76 Å length and short F···F contacts of 2.75−2.93 Å length are observed in **5**.

Magnetic Properties. Magnetic properties of salts **1**-**5** were studied by EPR spectroscopy and SQUID magnetometry on polycrystalline samples sealed in 2 mm quartz tubes under an argon atmosphere. All magnetic data are summarized in Table S9.

Salt **1** contains two paramagnetic species: high-spin $Mn^{II}(hfac)_3^-$ (S = 5/2) and $TSeT^{\bullet+}$ (S = 1/2). The $\chi_M T$ value is 4.28 emu·K/mol at 300 K. It is slightly smaller than the calculated value of 4.37 emu·K/mol for an isolated S = 5/2 spin at g = 2. Therefore, no contribution from $TSeT^{\bullet+}$ is observed. As a result, no coupling between the $Mn^{II}(hfac)_3^-$ anions is found since the salt shows paramagnetic behavior with the zero Weiss temperature (Figure S16). EPR signal from $TSeT^{\bullet+}$ is also not observed in the whole temperature range studied. The reason for that is the localization of positive charges on the dimers, whereas strong dimerization within these dimers provides their diamagnetism due to the antiparallel alignment of spins. Probably their triplet state can be populated above 300 K. Nevertheless, salt **1** shows an intense, broad EPR signal attributed to high-spin Mn^{II} showing zero-field splitting. The splitting of a signal is observed even at room temperature (295 K), and the isotropic g−factor is estimated to be 1.9910 (Figure S18). The signal can be approximated well by EasySpin program[44] with g_1 = 1.8672, g_2 = 1.7332, g_3 = 2.2802, g_{iso} = 1.9750, D = 0.0014, E = 0.0004 cm^{-1} at 6 K (Figure 7b). Therefore, the isotropic g-factor

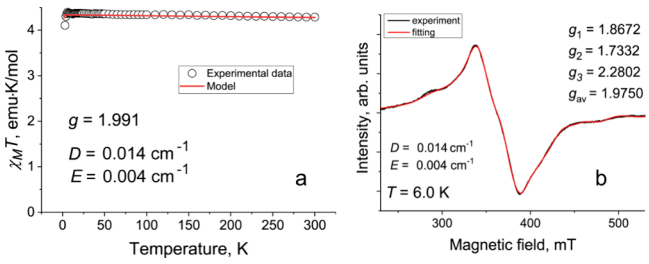

Figure 7. Magnetic data for $(TSeT_{1.5})^+\{Mn^{II}(hfac)_3^-\}$ (**1**): (a) temperature dependence of $\chi_M T$ values and fitting of the data by using PHI[45] (b) EPR spectrum of polycrystalline **1** at 6 K and fitting of the data by using EasySpin program.[44]

decreases with temperature. The obtained D and E parameters can be used for the fitting of the magnetic data by PHI.[41] The data can be approximated well with g = 1.9910 (Figure 6a). Magnetization of **1** is not saturated in a magnetic field up to 50 kOe, reaching the value of 4.90 $\mu_B N_A$ at 2 K. Such behavior is well described by PHI (Figure S17). Thus, spins from $TSeT^{\bullet+}$ are not observed in **1** due to dimerization, and that suppresses magnetic coupling between isolated high-spin $Mn^{II}(hfac)_3^-$ anions due to large distances between them.

A similar situation is observed for **2**, which also contains high-spin $Mn^{II}(hfac)_3^-$ (S = 5/2) and $TSeT^{\bullet+}$ (S = 1/2). The $\chi_M T$ value is 4.25 emu·K/mol at 300 K. It is slightly smaller than the calculated value for isolated S = 5/2 spin (4.37 emu·K/mol) at g = 2 (Figure S21). The Weiss temperature Θ = −2 K (Figure S20) supports weak antiferromagnetic coupling of spins. EPR spectrum of **2** was studied in the 4.2−295 K range. It shows a very broad EPR signal attributed to high-spin Mn^{II} with zero-field splitting. Narrow EPR signals that can be attributed to $TSeT^{\bullet+}$ or thioindigo$^{\bullet-}$ (these species can appear due to charge transfer (CT) from TSeT to thioindigo at their interaction within the layers) are also not observed. Therefore, the $TSeT^{\bullet+}$ species are not found due to the localization of positive electron density on the dimers and diamagnetism of these dimers due to antiparallel alignment of spins. CT from TSeT to thioindigo is also not observed. EPR spectrum of Mn^{II} can be fitted well by three Lorentzian lines at g_1 = 2.3177 (ΔH = 75.7 mT), g_2 = 1.9515 (ΔH = 65.1 mT), and g_3 = 1.6705 (ΔH = 85 mT) with isotropic g = 1.9975, and the zero field splitting parameter $|D|$ can be determined from the splitting as 0.0768 cm^{-1} (Figure S22). This parameter is directly determined from the spectra since the EasySpin program[44] does not allow it to be fitted well. Determined $|D|$ was used to fit magnetic data for **2** with g = 1.9667. This value is rather close to the isotropic g-factor determined from the EPR (g = 1.9975). The shape of the curve does not change visually when the sign of D is changed. Thus, salt **2** also contains only weakly interacting $Mn^{II}(hfac)_3^-$ anions due to the absence of spins on the TSeT sublattice.

Salt **3** contains the $Pr^{III}(hfac)_4^-$ anions and $TSeT^{\bullet+}$ arranged in the stacks. Pr^{III} has a $^3H_4$ state at g = 4/5.[46] The $\chi_M T$ value for **3** is 1.66 emu·K/mol at 300 K. The $\chi_M T$ value calculated for the isolated Pr^{III} ion is 1.60 emu·K/mol, whereas the additional contribution from $TSeT^{\bullet+}$ (S = 1/2) increases this value up to 1.66 emu·K/mol. The observed value is closer to that of the system when both paramagnetic species contribute to susceptibility. The temperature dependence for $\chi_M T$ values is shown in Figure S25. A decrease in these values with temperature down to 0.25 emu·K/mol at 2 K indicates a rather strong antiferromagnetic coupling of spins. The Weiss temperature θ = −7 K (Figure S24) supports this supposition. Therefore, the preservation of spins on the TSeT sublattice yields rather strong antiferromagnetic coupling between the Pr^{III} spins despite the large distances between them (12.48 Å). Nevertheless, the exact exchange between Pr^{III} cannot be estimated by PHI due to the essential orbital contribution characteristic of Pr^{III}. We performed AC measurements for **3** at applied external DC field up to 5000 Oe and observed no out-of-phase signals on the $\chi''(\nu)$ dependence, indicating the absence of SIM properties in contrast to previously studied $(TSeT_{1.5})^+\{Dy^{III}(hfac)_4^-\}$, which is field-induced SIM.[26] The $\{Er^{III}(hfac)_4^-\}$ anions can show SIM properties.[24] However, no crystals were obtained in the synthesis with TSeT and $Er^{III}(hfac)_3$. Though the EPR signal from Pr^{III} is not observed, the contribution from $TSeT^{\bullet+}$ is well seen in EPR. Different behavior of the EPR signals manifests itself in two temperature ranges. A broad Lorentzian signal is observed in the 180−300 K range with g = 2.0250 and the line width ΔH = 9.66 mT at 295 K (Figure 8a). This signal narrows with the temperature decrease, but the g-factor is temperature independent (Figure 8d,e). Spectrum **3** also contains a weak narrow signal (Figure 8a) with g = 2.0003 and ΔH = 0.6 mT. The integral intensity of this signal is less than <1% of that of the broad signal and can be attributed to paramagnetic impurities. Intensity of the broad signal grows above 180 K with the temperature increase, indicating that it can be attributed to thermal population of the excited triplet state in the dimers. A plot of natural logarithm of integral intensity after the subtraction of integral intensity of the signal below 180 K vs reverse temperature allows the estimation of a singlet−triplet gap as 420 K. Similar behavior was previously found for $(TSeT_{1.5})^+\{Dy^{III}(hfac)_4^-\}$ which showed a singlet−triplet gap of 542 K.[26] Thermal population of the excited triplet state of the dimer above 180 K is

https://doi.org/10.1021/acs.cgd.5c00737
Cryst. Growth Des. 2025, 25, 6332−6344

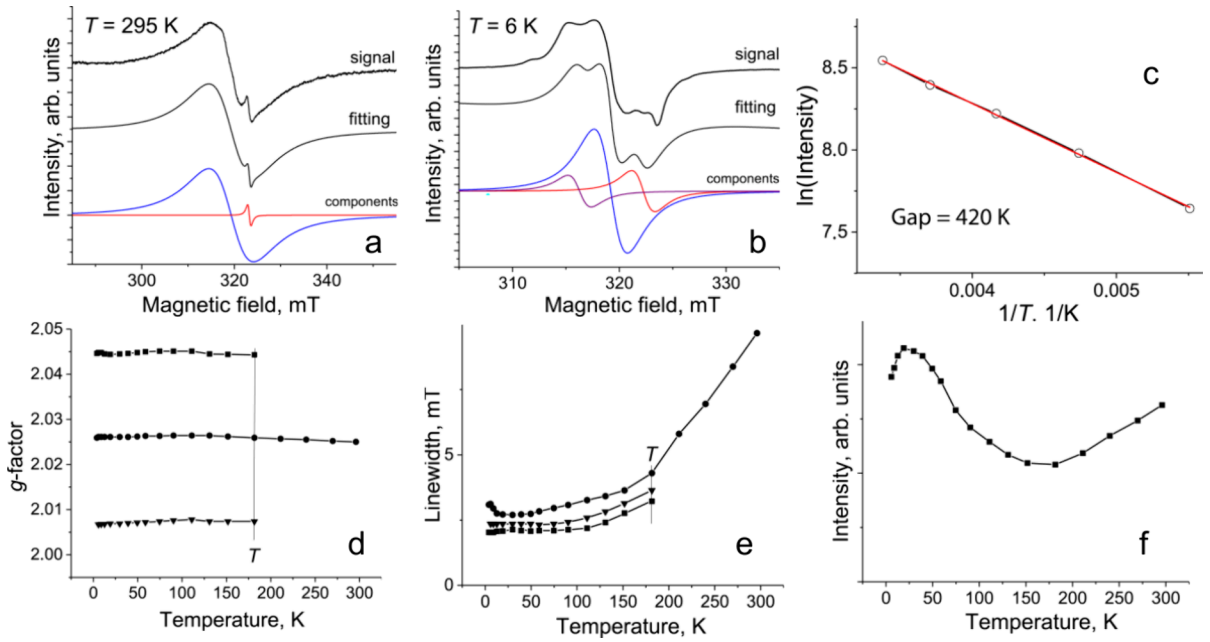

Figure 8. EPR data: spectra of polycrystalline $(TSeT_{1.5})^{+}\{Pr^{III}(hfac)_4^{-}\}$ (**3**) at room temperature (295 K, a); 6 K (b) fitting of these spectra by several Lorentzian lines is shown below; the dependence of natural logarithm of intensity versus reverse temperature for the EPR signal from $TSeT^{\bullet+}$ in the 180−300 K range which allows the determination of singlet−triplet gap in the dimers (c); temperature dependences of *g*-factor (d), line width (e), and total integral intensity (f) of the lines. *T* shows the temperature of splitting of the EPR signal from $TSeT^{\bullet+}$ into three lines.

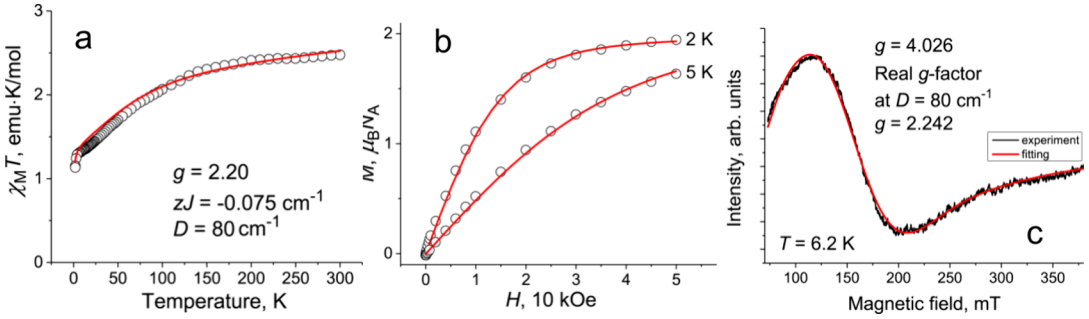

Figure 9. (a) Temperature dependence of $\chi_M T$ for polycrystalline $(TSeT_2)^{+}\{Co^{II}(hfac)_2Cl^{-}\}$ (**4**) and fitting of the data by PHI[39] (red curve); (b) dependence of magnetization vs magnetic field (open circles) up to 50 kOe magnetic field at 2 and 5 K and fitting of the data by PHI[45] (red curve); (c) EPR signal from **4** at 6.2 K and fitting of the signal by EasySpin program[44] (red curve).

accompanied by the increase in the $\chi_M T$ value from 1.60 emu·K/mol (160 K) to 1.66 emu·K/mol (300 K). The $\chi_M T$ value below 180 K is even closer to the contribution of only one independent Pr^{III} ion. However, the EPR signal is also preserved in the 180−4.2 K range. It can be attributed to paramagnetic $TSeT^{\bullet+}$ monomers. The behavior of this signal is completely different from that of the broad signal. It splits into three components due to asymmetry (Figure 8b). These components are only slightly narrowed with the temperature decrease and have temperature-independent *g*-factors (Figure 8d,e). As a result, the split signal has the following parameters at 6 K: $g_1 = 2.0446$ ($\Delta H = 2.02$ mT), $g_2 = 2.0261$ ($\Delta H = 3.12$ mT), and $g_3 = 2.0067$ ($\Delta H = 2.35$ mT) (Figure 8b). The total integral intensity of the split signal increases with the temperature decrease down to 20 K, below which the drop in intensity is observed. Spins of the $TSeT^{\bullet+}$ monomers are probably involved in the antiferromagnetic coupling with $Pr^{III}(hfac)_4^{-}$. Thus, weaker dimerization in the TSeT stacks preserves the spin density on the monomers, whereas the triplet state of the dimers is populated above 180 K. The appearance of spins on the TSeT sublattice provides rather strong antiferromagnetic coupling between $Pr^{III}(hfac)_4^{-}$ anions, which most probably also involves $TSeT^{\bullet+}$.

Salt **4** contains high-spin $Co^{II}(hfac)_2Cl^{-}$ ($S = 3/2$) and $TSeT^{\bullet+}$ ($S = 1/2$). The $\chi_M T$ value is 2.46 emu·K/mol at 300 K (Figure 9a). This value is essentially higher than the 1.87 emu·K/mol expected for an isolated $S = 3/2$ spin at $g = 2.0$. Generally, that is due to the essential spin−orbit contribution of high-spin Co^{II} ions. The contribution of $TSeT^{\bullet+}$ cannot be resolved in this case. Nevertheless, a very broad EPR signal is observed only below 50 K, and such behavior is expected for high-spin Co^{II} with short relaxation times.[47] A narrow EPR signal, which can be attributed to $TSeT^{\bullet+}$, is not found in the whole temperature range, indicating that the spins of all these species are paired in the dimers. Indeed, salt **4** shows dimerization within the stacks, with very short interplanar distances within the dimers. Positive charge is localized mainly on the dimers according to the Se−Se bond length. As a result, spins are aligned antiparallel in the dimers below 300 K. The $\{Co^{II}(hfac)_2Cl^{-}\}_2$ dimers are formed in **4** with an intermolecular Co^{II} distance of 7.36 Å. However, the distance between the planar parts of hfac is rather long (4.17 Å), and no van der

https://doi.org/10.1021/acs.cgd.5c00737
Cryst. Growth Des. 2025, 25, 6332−6344

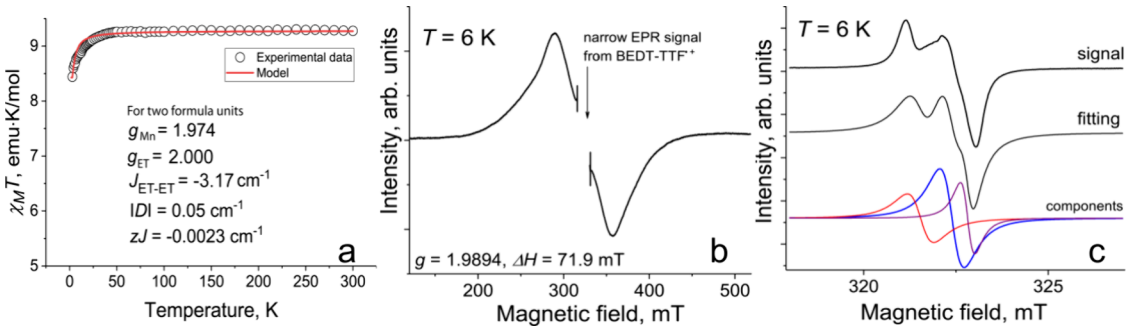

Figure 10. (a) Temperature dependence of $\chi_M T$ for polycrystalline (BEDT-TTF$_3$)$^+${Mn^{II}(hfac)$_3^-$} (**5**) and fitting of the data by PHI program[45] (red curve, parameters of fitting are shown below); (b) EPR signal for polycrystalline **4** from high-spin Mn^{II} at 6 K (the range where the intense narrow EPR signal from BEDT-TTF$^{\bullet+}$ is manifested is not shown); (c) EPR signal from BEDT-TTF$^{\bullet+}$ at 6 K and fitting of these signal by three Lorentzian lines).

Waals contacts are formed between them. Therefore, we modeled the magnetic behavior of **4** per formula unit and isolated Co^{II}(hfac)$_2$Cl$^-$ anions. The $\chi_M T$ values decrease even below 300 K, and such behavior can be described only by the very strong zero-field splitting of D = 80 cm^{-1} at g = 2.20. Weak antiferromagnetic coupling between Co^{II} ions can be taken into account using small intermolecular antiferromagnetic coupling of zJ = −0.075 cm^{-1} (Figure 9a). We also tried to fit the data into two formula units to estimate the J_{Co-Co} coupling. However, in this case, J_{Co-Co} is also very low, whereas the D value is high, but better correspondence between theoretical and experimental curves was found when antiferromagnetic Co−Co coupling was modeled by using zJ. The Weiss temperature is negative (Θ = −15 K) (Figure S27), but most probably that is due to a very high D value. The most valuable evidence of a high positive parameter D can be obtained from the simultaneous fitting of magnetization at 2 and 5 K. The very close correspondence between theoretical and experimental curves (Figure 9b) indicates that parameter D was determined correctly. Magnetization is not saturated up to 50 kOe, attaining values of 1.93 and 1.67 $\mu_B N_A$ at 2 and 5 K, respectively (Figure 9b). Salt **4** shows a broad EPR signal below 50 K, as expected for high-spin Co^{II}. The signal has g = 4.0042 and ΔH = 66.9 mT at 50 K (Figure S28). It shifts to g = 4.026 and broadens to 94.6 mT at 6.2 K (Figure 9c). Taking into account the very high D value (80 cm^{-1}), the correctly calculated g-factor value is 2.2422, that is close to g = 2.20 obtained from the fitting of $\chi_M T$ (Figure 9a). That also confirms the correct determination of the D value. We performed AC measurements for **4** at an applied external DC field up to 5000 Oe, but we observed no out-of-phase signals on the $\chi''(\nu)$ dependence in the 1−1500 Hz range.

Salt **5** contains isolated high-spin Mn^{II}(hfac)$_3^-$ (S = 5/2) and BEDT-TTF$^{\bullet+}$ (abbreviation is ET) in the layers (total charge +1 and one S = 1/2 spin per formula unit). To estimate magnetic coupling between Mn^{II}, we calculated magnetic data per two formula units. The $\chi_M T$ value is 9.28 emu·K/mol at 300 K (Figure 10a). That is only slightly lower than the value of 9.50 emu·K/mol calculated per two formula units with two independent S = 5/2 and 1/2 spins at g = 2. The Weiss temperature of Θ = −2 K indicates weak antiferromagnetic coupling of spins. Three types of magnetic exchange are possible in **5**: J_{Mn-Mn}, J_{Mn-ET}, and J_{ET-ET}. Magnetic data were fitted by PHI[39] with g_{Mn}= 1.9742, g_{ET} = 2.0000, small zero-field splitting parameter |D| = 0.5 cm^{-1}. $J_{Mn-Mn,\ Mn-ET}$ coupling is close to zero, whereas J_{ET-ET} coupling is equal to −3.17 cm^{-1}. Antiferromagnetic coupling, except for the J_{ET-ET} coupling, can be taken into account by using the averaged intermolecular antiferromagnetic coupling of zJ = −0.0023 cm^{-1} (Figure 10a). Thus, weak coupling is observed only in the BEDT-TTF layers. Magnetization is not saturated up to 50 kOe magnetic field, attaining the value of 10.13 $\mu_B N_A$ at 2 K. Such behavior is described well by PHI with the same parameters (Figure S31). EPR spectrum of **5** contains a very broad signal from Mn^{II} on the background of an intense narrow signal from BEDT-TTF$^{\bullet+}$. The first signal can be described by one Lorentzian line with g = 2.0054 mT (ΔH = 68.4 mT) at 295 K (Figure S32), and the signal shifts to smaller g-factors with the temperature decrease (g = 1.9894, ΔH = 71.9 mT at 6 K, Figure 10b). The narrow signal from BEDT-TTF$^{\bullet+}$ can be described by two Lorentzian lines with g_1 = 2.0084 (ΔH = 0.92 mT) and g_2 = 2.0048 (ΔH = 0.72 mT) at 295 K (Figure S33), and the signal splits even more strongly with a temperature decrease (Figures S34 and S35). It can be described by three Lorentzian lines with g_1 = 2.0114 (ΔH = 0.72 mT), g_2 = 2.0061 (ΔH = 0.46 mT), and g_3 = 2.0035 (ΔH = 0.38 mT) at 6 K (Figure 10c). As we showed in the Crystal structure section, positive charge and correspondingly spin are localized mainly on one of three BEDT-TTF molecules within the layers. Weak coupling between BEDT-TTF$^{\bullet+}$ in the layers can most probably be mediated through the neighboring BEDT-TTF molecules, whereas exchange between high-spin Mn^{II}(hfac)$_3^-$ anions is suppressed.

Conductivity Measurements for 3 and Theoretical Calculations. Conductivity of **3** was measured by a four-probe technique for a single crystal oriented by X-ray diffraction in such a way that it was measured along the conducting 1D stacks from the TSeT molecules and along the crystallographic a-axis. A single crystal shows semiconducting behavior with an estimated activation energy of 83 meV (the determination of this energy is given in Figure S36). This energy is slightly lower than that in (TSeT$_{1.5}$)$^+${Dy^{III}(hfac)$_4^-$} (91 meV),[26] probably due to a smaller singlet−triplet gap for the dimers in **3** (420 K) in comparison with the Dy^{III} compound (542 K).

Electronic properties of the conducting stacks composed of the TSeT molecules in **3** were determined using the Extended Hückel method[48,49] based on the data of X-ray diffraction collected for a single crystal of **3** at room temperature. Figure 11 shows the calculated band structure for crystal orbitals with energies, which are close to the Fermi level (E_F = −4.524 eV) within the E_F ± 1.5 eV range, and total density of states

https://doi.org/10.1021/acs.cgd.5c00737
Cryst. Growth Des. 2025, 25, 6332−6344

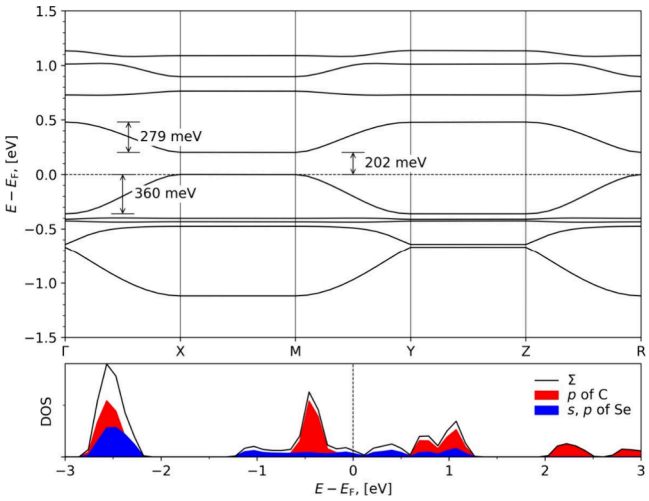

Figure 11. Band diagram of the 1D stacks of TSeT in **3**.

(DOS). According to the structure of **3**, the TSeT stacks are oriented along the crystallographic *a* axis, which corresponds to the Γ(0,0,0)−X(1/2,0,0) path in reciprocal space (see Figure 11). The lowest unoccupied electronic band has a width of ∼279 meV, and the highest occupied band has a width of 360 meV. It can be concluded from the comparison with the previous data[26] that such widths are typical for TSeT-based crystals. The analysis of conductivity shows semiconducting behavior due to weak dimerization of the stacks, and such a character of conductivity is supported by direct conductivity measurements by a four-probe technique. Room-temperature specific electrical resistance $\rho_{\parallel}$ = 200 Ohm·cm along the chains and $\rho_{\perp} = 2.3 \times 10^7$ Ohm·cm across the chains. Therefore, $\rho_{\perp}/\rho_{\parallel}$ anisotropy is 1.15×10^5. The conductivity of crystals of other salts was measured by a two-probe technique at room temperature, and all of them showed rather high resistivity ($R > 10^8$ Ohm). These conditions do not allow for correct measurements of temperature dependences of resistivity.

CONCLUSIONS

A new method for the preparation of tetraselenatetracene and bis(etheleneditio)tetrathiafulvalene salts with paramagnetic anions based on hexafluoroacetylacetonates of Mn^{II}, Co^{II}, and Pr^{III} has been developed. Hexafluoroacetylacetonates add one more hfac ligand, forming bulk $\{Mn^{II}(hfac)_3\}^-$ and $[Pr^{III}(hfac)_4]^-$ anions when TSeT and BEDT-TTF are oxidized. The formation of $Co^{II}(hfac)_2Cl^-$ in **4** is not described by this scheme, and most probably this anion is formed when $Co^{II}(hfac)_2$ abstracts the chloride anion from the solvent $C_6H_4Cl_2$ molecules. The possibility for the introduction of dye molecules into the TSeT salts is shown to be due to a close approach of an acceptor carbonyl oxygen atom to the center of a Se−Se bond. As a result, short Se···O contacts are formed. Bulk anions provide high solubility of these salts even in nonpolar solvents. However, their large size provides some peculiarities in the packing mode of radical cations and paramagnetic anions. TSeT and BEDT-TTF molecules form 1D π-stacks and 2D layers, respectively. The formal charge on the donor molecules is rather low, ranging from +0.333 to +0.666. The TSeT molecules dimerize within the stacks, and the positive charge is localized mainly on the dimers. Since the TSeT molecules are closely packed in these dimers, spins are aligned antiparallel to each other in the dimers, preserving their diamagnetic singlet state up to room temperature. The BEDT-TTF layers show positive charge localization on one of three molecules. As a result, weak antiferromagnetic coupling is observed in the BEDT-TTF layers. The absence of spins on the TSeT stacks in **1** and **2** and shielding of the BEDT-TTF$^{\bullet+}$ cations from $\{Mn^{II}(hfac)_3\}^-$ by the $-CH_2-CH_2-$ groups in **5** magnetically isolate $\{Mn^{II}(hfac)_3\}^-$ anions in the salts. An exception from this tendency is salt **3** with $[Pr^{III}(hfac)_4]^-$, which contains weakly dimerized stacks. As a result, charge is localized on both monomers and dimers, and the triplet state of the dimers is populated above 180 K. Since charge carriers appear on the TSeT stacks above this temperature, the salt is semiconducting. Most probably, TSeT monomers are involved in the antiferromagnetic coupling of spins observed between Pr^{III} ions at low temperatures. Co^{II} positioned in a square pyramidal surrounding has a high zero-field splitting parameter *D*. However, SIM properties were not found for $(TSeT_2)^+\{Co^{II}(hfac)_2Cl^-\}$ (**4**). Probably, the use of other donors, which can form more uniform stacks, can solve the problem of dimerization, whereas delocalization of the electron density over the 2D layers is needed for the manifestation of conductivity in the BEDT-TTF layers. Hexafluoroacetylacetonate anions with SIM properties[26,43] can introduce magnetism in these salts. This work is in progress.

ASSOCIATED CONTENT

Supporting Information

The Supporting Information is available free of charge at https://pubs.acs.org/doi/10.1021/acs.cgd.5c00737.

Table S1−S5 and Figures S1−S5: IR spectra and their description, Figures S6 and S7: optical spectra; Figures S8−S12: IR spectra in the 400−7000 cm^{-1} range which show charge transfer bands; Figures S13 and S14 and Tables S6−S8: crystal structure and analysis of the metal surrounding by Shape software; Figures S15−S35: DC SQUID and EPR measurements; Figure S36: Conductivity measurements on oriented single crystal (PDF)

Accession Codes

Deposition Numbers 2422843 and 2433183−2433186 contain the supplementary crystallographic data for this paper. These data can be obtained free of charge via the joint Cambridge Crystallographic Data Centre (CCDC) and Fachinformationszentrum Karlsruhe Access Structures service.

AUTHOR INFORMATION

Corresponding Author

Dmitri V. Konarev − *Federal Research Center of Problems of Chemical Physics and Medicinal Chemistry RAS, Chernogolovka, Moscow Region 142432, Russia;* orcid.org/0000-0002-7326-8118; Phone: +007-9153137550; Email: konarev3@yandex.ru

Authors

Alexandra M. Flakina − *Federal Research Center of Problems of Chemical Physics and Medicinal Chemistry RAS, Chernogolovka, Moscow Region 142432, Russia*

Dmitry I. Nazarov − *Federal Research Center of Problems of Chemical Physics and Medicinal Chemistry RAS, Chernogolovka, Moscow Region 142432, Russia*

Maxim A. Faraonov − *Federal Research Center of Problems of Chemical Physics and Medicinal Chemistry RAS,*

https://doi.org/10.1021/acs.cgd.5c00737
Cryst. Growth Des. 2025, 25, 6332−6344

Chernogolovka, Moscow Region 142432, Russia; orcid.org/0000-0003-0805-601X

Aleksey V. Kuzmin – *Institute of Solid State Physics RAS, Chernogolovka, Moscow Region 142432, Russia*

Eleonora I. Khasanova – *Institute of Solid State Physics RAS, Chernogolovka, Moscow Region 142432, Russia*

Ilya A. Yakushev – *Kurnakov Institute of General and Inorganic Chemistry, Russian Academy of Sciences, Moscow 119991, Russia*

Vladimir N. Zverev – *Institute of Solid State Physics RAS, Chernogolovka, Moscow Region 142432, Russia*

Akihiro Otsuka – *Division of Chemistry, Graduate School of Science, Kyoto University, Kyoto 606-8502, Japan;* orcid.org/0000-0002-3141-0702

Hiroshi Kitagawa – *Division of Chemistry, Graduate School of Science, Kyoto University, Kyoto 606-8502, Japan;* orcid.org/0000-0001-6955-3015

Complete contact information is available at: https://pubs.acs.org/10.1021/acs.cgd.5c00737

Funding

The preparation and study of **1**-5 was supported by the Russian Science Foundation (project N 24-13-00060). The IR absorption study was supported by the Ministry of Science and Higher Education of the Russian Federation (Registration numbers 124013100858-3). Some magnetic measurements were supported by JSPS KAKENHI, Grant Numbers JP20H05623, and JP22H23425. Theoretical calculations were supported in part through computational resources of HPC facilities at NRU HSE.

Notes

The authors declare no competing financial interest.

REFERENCES

(1) Coronado, E.; Galan-Mascaros, J. R.; Gomez-Garcia, C. J.; Laukhin, V. Coexistence of ferromagnetism and metallic conductivity in a molecule-based layered compound. *Nature* **2000**, *408*, 447−449.

(2) Gonzalez, M. I.; Turkiewicz, A. B.; Darago, L. E.; Oktawiec, J.; Bustillo, K.; Grandjean, F.; Long, G. J.; Long, J. R. Confinement of atomically defined metal halide sheets in a metal-organic framework. *Nature* **2020**, *577*, 64−68.

(3) Naito, T. Modern history of organic conductors: an overview. *Crystals* **2021**, *11*, 838.

(4) Williams, J. M.; Ferraro, J. R.; Thorn, R. J.; Carlson, K. D.; Geiser, U.; Wang, H. H.; Kini, A. M.; Whangbo, M. H.; Organic Superconductors (Including Fullerenes). In *Synthesis, Structure, Properties and Theory*; Prentice Hall: Englewood Cliffs, NJ, USA, 1992.

(5) Saito, G.; Yoshida, Y. Development of conductive organic molecular assemblies: organic metals, superconductors, and exotic functional materials. *Bull. Chem. Soc. Jpn.* **2007**, *80*, 1−137.

(6) Sessoli, R.; Gatteschi, D.; Caneschi, A.; Novak, M. A. Magnetic bistability in a metal-ion cluster. *Nature* **1993**, *365*, 141−143.

(7) Rinehart, J. D.; Fang, M.; Evans, W. J.; Long, J. R. A N_2(3-) radical-bridged terbium complex exhibiting magnetic hysteresis at 14 K. *J. Am. Chem. Soc.* **2011**, *133*, 14236−14239.

(8) Guo, F. S.; Day, B. M.; Chen, Y. C.; Tong, M. L.; Mansikkamaki, A.; Layfield, R. A. A dysprosium metallocene single-molecule magnet functioning at the axial limit. *Angew. Chem., Int. Ed.* **2020**, *59*, 18844−18844.

(9) Goodwin, C. A. P.; Ortu, F.; Reta, D.; Chilton, N. F.; Mills, D. P. Molecular magnetic hysteresis at 60 K in dysprosium. *Nature* **2017**, *548*, 439−442.

(10) Hanasaki, N.; Tajima, H.; Matsuda, M.; Naito, T.; Inabe, T. Giant negative magnetoresistance in quasi-one-dimensional conductor TPP[Fe(Pc)(CN)$_2$]$_2$: Interplay between local moments and one-dimensional conduction electrons. *Phys. Rev. B: Condens. Matter* **2000**, *62*, 5839−5842.

(11) Kubo, K.; Shiga, T.; Yamamoto, T.; Tajima, A.; Moriwaki, T.; Ikemoto, Y.; Yamashita, M.; Sessini, E.; Mercuri, M. L.; Deplano, P.; Nakazawa, Y.; Kato, R. Electronic state of a conducting single molecule magnet based on Mn-salen type and Ni-dithiolene complexes. *Inorg. Chem.* **2011**, *50*, 9337−9344.

(12) Shen, Y. B.; Cosquer, G.; Ito, H.; Izuogu, D. C.; Thom, A. J. W.; Ina, T.; Uruga, T.; Yoshida, T.; Takaishi, S.; Breedlove, B. K.; Li, Z. Y.; Yamashita, M. An organic-inorganic hybrid exhibiting electrical conduction and single-ion magnetism. *Angew. Chem., Int. Ed.* **2020**, *59*, 2399−2406.

(13) Shen, Y. B.; Ito, H.; Zhang, H. T.; Yamochi, H.; Katagiri, S.; Yoshina, S. K.; Otsuka, A.; Ishikawa, M.; Cosquer, G.; Uchida, K.; Herrmann, C.; Yoshida, T.; Breedlove, B. K.; Yamashita, M. Simultaneous manifestation of metallic conductivity and single molecule magnetism in a layered molecule-based compound. *Chem. Sci.* **2020**, *11*, 11154−11161.

(14) Shen, Y.; Ito, H.; Zhang, H.; Yamochi, H.; Cosquer, G.; Herrmann, C.; Ina, T.; Yoshina, S. K.; Breedlove, B. K.; Otsuka, A.; Ishikawa, M.; Yoshida, T.; Yamashita, M. emergence of metallic conduction and cobalt(II)-based single-molecule magnetism in the same temperature range. *J. Am. Chem. Soc.* **2021**, *143*, 4891−4895.

(15) Kushch, N. D.; Buravov, L. I.; Kushch, P. P.; Shilov, G. V.; Yamochi, H.; Ishikawa, M.; Otsuka, A.; Shakin, A. A.; Maximova, O. V.; Volkova, O. S.; Vasiliev, A. N.; Yagubskii, E. B. Multifunctional compound combining conductivity and single-molecule magnetism in the same temperature range. *Inorg. Chem.* **2018**, *57*, 2386−2389.

(16) Flakina, A. M.; Zhilyaeva, E. I.; Shilov, G. V.; Faraonov, M. A.; Torunova, S. A.; Konarev, D. V. Layered organic conductors based on BEDT-TTF and Ho, Dy, Tb chlorides. *Magnetochemistry* **2022**, *8*, 142.

(17) Shen, Y. B.; Cosquer, G.; Breedlove, B. K.; Yamashita, M. Hybrid molecular compound exhibiting slow magnetic relaxation and electrical conductivity. *Magnetochemistry* **2016**, *2*, 44.

(18) Caneschi, A.; Gatteschi, D.; Sessoli, R. Magnetic properties of a layered molecular material comprising manganese hexafluoroacetylacetonate and nitronyl nitroxide radicals. *Inorg. Chem.* **1993**, *32*, 4612−4616.

(19) Meng, X.; Shi, W.; Cheng, P. Magnetism in one-dimensional metal−nitronyl nitroxide radical system. *Coord. Chem. Rev.* **2019**, *378*, 134−150.

(20) Artiukhova, N. A.; Romanenko, G. V.; Bogomyakov, A. S.; Barskaya, I. Yu.; Veber, S. L.; Fedin, M. V.; Maryunina, K. Yu.; Inoue, K.; Ovcharenko, V. I. Cu(ii) complex with nitronyl nitroxide whose paramagnetism is suppressed by temperature decrease and/or pressure increase. *J. Mater. Chem. C* **2016**, *4*, 11157−11163.

(21) Osipov, N. G.; Faraonov, M. A.; Shestakov, A. F.; Mikhailenko, M. V.; Kuzmin, A. V.; Khasanov, S. S.; Otsuka, A.; Yamochi, H.; Kitagawa, H.; Konarev, D. V. Binuclear coordination complex of open merocyanine form of photochromic spiropyran with $Mn^{II}(hfac)_2$ having high spin (S = 5) ground state. *New J. Chem.* **2023**, *47*, 5470−5476.

(22) Osipov, N. G.; Faraonov, M. A.; Yakushev, I. A.; Denisov, N. N.; Otsuka, A.; Kitagawa, H.; Konarev, D. V. Slow magnetic relaxation in a complex of photochromic spiropyran in merocyanine form and cobalt(II) hexafluoroacetylacetonate. *Dalton Trans.* **2024**, *53*, 3159−3166.

(23) Galangau, O.; Flores Gonzalez, J.; Montigaud, V.; Dorcet, V.; Le Guennic, B.; Cador, O.; Pointillart, F. Dysprosium Single-Molecule Magnets Involving 1,10-Phenantroline-5,6-Dione Ligand. *Magnetochemistry* **2020**, *6*, 19.

(24) Prokhorova, T. G.; Korchagin, D. V.; Shilov, G. V.; Dmitriev, A. I.; Zhidkov, M. V.; Yagubskii, E. B. The organic ammonium counterion effect on slow magnetic relaxation of the $[Er(hfac)_4]^-$ complexes. *Magnetochemistry* **2023**, *9*, 159.

(25) Shtefanets, V. P.; Shilov, G. V.; Yurieva, E. A.; Babeshkin, K. A.; Efimov, N. N.; Sanina, N. A.; Aldoshin, S. M. Mutual influence of

photochromic and magnetic sublattices in crystals of erbium(III) tetrakis(hexafluoroacetylacetonate) salt with 1-[(1′,3′,3′-trimethylspiro[2i/-1-benzopyran-2,2′-indoline]-8-yl)methyl]-pyridinium. *Inorg. Chim. Acta* **2025**, *585*, No. 122755.
(26) Flakina, A. M.; Nazarov, D. I.; Faraonov, M. A.; Yakushev, I. A.; Kuzmin, A. V.; Khasanov, S. S.; Zverev, V. N.; Otsuka, A.; Yamochi, H.; Kitagawa, H.; Konarev, D. V. Single ion magnetism of the $[Dy^{III}(hfac)_4]^-$ anions in crystalline semiconductor $\{TSeT_{1.5}\}^{\bullet+}[Dy^{III}(hfac)_4]^-$ containing weakly dimerized stacks of tetraselenatetracene. *Int. J. Mol. Sci.* **2024**, *25*, 8068.
(27) Balodis, K. A.; Livdane, A. D.; Medne, R. S.; Neiland, O. Y. Preparation of tetraselenotetracene from 5,6,11,12-tetrachlorotetracene and sodium diselenide. *Zh. Org. Khim.* **1979**, *15* (N. 2), 391–393.
(28) Bruker *APEX3, SAINT and SADABS*; Bruker AXS Inc.: Madison, **2016**
(29) Sheldrick, G. M. A short history of *SHELX*. *Acta Crystallogr: Sec. A Found Crystallogr.* **2008**, *64*, 112–122.
(30) Dolomanov, O. V.; Bourhis, L. J.; Gildea, R. J.; Howard, J. A. K.; Puschmann, H. OLEX2: a complete structure solution, refinement and analysis program. *J. Appl. Crystallogr.* **2009**, *42*, 339–341.
(31) Raebiger, J. W.; Miller, J. S. Magnetic ordering in the rare earth molecule-based magnets, $Ln(TCNE)_3$ (Ln = Gd, Dy; TCNE is tetracyanoethylene). *Inorg. Chem.* **2002**, *41*, 3308–3312.
(32) Nazarov, D. I.; Rompanen, I. A.; Khasanov, S. S.; Ivanov, E. N.; Koifman, O. I.; Islyaikin, M. K.; Konarev, D. V. Preparation of $\{Cryptand(Li^+)\}_2\{Li_3(Cl^-)(Hhp)\}_2 \cdot 6C_6H_4Cl_2$ and $\{Cryptand(Li^+)\}\{H_2TPCor^-\}\cdot 0.5C_6H_4Cl_2$ by deprotonation of free-base trithiodode-caazahexaphyrin (H_3Hhp) and triphenylcorrole (H_3TPCor) macrocycles. *Polyhedron* **2021**, *202*, No. 115198.
(33) Zolotukhin, S. P.; Kaminskii, V. F.; Kotov, A. I.; Khidekel', M. L.; Shibaeva, R. P.; Yagubskii, E. B. Studies in the field of organic metals 3. Nonstoichiometric tetraselenotetracene iodides. *Bull. Acad. Sci. USSR Div. Chem. Sci.* **1978**, *27*, 1590–1595.
(34) Kaminskii, V. F.; Kostuchenko, E. E.; Shibaeva, R. P.; Yagubskii, E. B.; Zvarykina, A. V. Quasi-one-dimentional conductors based on tetrathiatetracene (TTT) and Tetraselenatetracene (TSeT) with metal complex mercury anions: synthesis, structure, properties. *J. Phys. Colloques* **1983**, *44* (C3), 1167–1181.
(35) Flakina, A. M.; Chekhlov, A. N.; Kaplunov, M. G.; Van, K. V.; Lyubovskaya, R. N. BEDT-TTF-based radical cation salt with the cyanurate anion: synthesis, structure, conductivity, and polarized reflection spectra. *Russ. Chem. Bull.* **2008**, *57*, 99–104.
(36) Guionneau, P.; Chasseau, D.; Howard, J. A. K.; Day, P. Neutral bis(ethylenedithio)tetrathiafulvalene at 100 K. *Acta Crystallogr.* **2000**, *C56*, 453–454.
(37) Brooks, A. C.; Martin, L.; Day, P.; Lopes, E. B.; Almeida, M.; Kikuchi, K.; Fujita, W.; Sasamori, K.; Aktusu, H.; Wallis, J. D. Hydrogen bonded anion ribbons, networks and clusters and sulfur–anion interactions in novel radical cation salts of BEDT-TTF with sulfamate, pentaborate and bromide. *Dalton Trans.* **2013**, *42*, 6645–6654.
(38) Llunell, M.; Casanova, D.; Cirera, J.; Alemany, P.; Alvarez, S.; *Program SHAPE*, Version 2.1; University of Barcelona: Spain, March 2013.
(39) Pinsky, M.; Avnir, D. Continuous symmetry measures. 5. The classical polyhedra. *Inorg. Chem.* **1998**, *37*, 5575–5582.
(40) Chopra, D.; Guru Row, T. N. Role of organic fluorine in crystal engineering. *CrystEngComm* **2011**, *13*, 2175–2186.
(41) Dey, D.; Bhandary, S.; Thomas, S. P.; Spackman, M. A.; Chopra, D. Energy frameworks and a topological analysis of the supramolecular features in in situ cryocrystallized liquids: tuning the weak interaction landscape via fluorination. *Phys. Chem. Chem. Phys.* **2016**, *18*, 31811–31820.
(42) Ho, P. C.; Wang, J. Z.; Meloni, F.; Vargas-Baca, I. Chalcogen bonding in materials chemistry. *Coord. Chem. Rev.* **2020**, *422*, No. 213464.
(43) Fourmigué, M.; Dhaka, A. Chalcogen bonding in crystalline diselenides and selenocyanates: From molecules of pharmaceutical interest to conducting materials. *Coord. Chem. Rev.* **2020**, *403*, No. 213084.
(44) Stoll, S.; Schweiger, A. EasySpin, a comprehensive software package for spectral simulation and analysis in EPR. *J. Magn. Reson.* **2006**, *178*, 42–55.
(45) Chilton, N. F.; Anderson, R. P.; Turner, L. D.; Soncini, A.; Murray, K. S. PHI: a powerful new program for the analysis of anisotropic monomeric and exchange-coupled polynuclear d- and f-block complexes. *J. Comput. Chem.* **2013**, *34*, 1164–1175.
(46) Benelli, C.; Gatteschi, D. Magnetism of lanthanides in molecular materials with transition-metal ions and organic radicals. *Chem. Rev.* **2002**, *102*, 2369–2388.
(47) Jankovics, H.; Daskalakis, M.; Raptopoulou, C. P.; Terzis, A.; Tangoulis, V.; Giapintzakis, J.; Kiss, T.; Salifoglou, A. Synthesis and structural and spectroscopic characterization of a complex between Co(II) and imino-bis(methylphosphonic acid): gaining insight into biologically relevant metal–ion phosphonate interactions or looking at a new Co(II)–organophosphonate material? *Inorg. Chem.* **2002**, *41*, 3366–3374.
(48) Hoffmann, R. An Extended Hückel Theory. *I. Hydrocarbons. J. Chem. Phys.* **1963**, *39*, 1397–1412.
(49) Ren, J.; Whangbo, M.-H. *CAESAR 2.0*; Primecolor Software, Inc.: Madison, WI, 1998

https://doi.org/10.1021/acs.cgd.5c00737
Cryst. Growth Des. 2025, 25, 6332–6344